





Article

Improving the Seasonal Representation of ASCAT Soil Moisture and Vegetation Dynamics in a Temperate Climate

Isabella Pfeil ^{1,2,*} , Mariette Vreugdenhil ², Sebastian Hahn ² , Wolfgang Wagner ^{1,2} , Peter Strauss ³  and Günter Blöschl ¹

¹ Centre for Water Resource Systems, TU Wien, 1040 Vienna, Austria;

wolfgang.wagner@geo.tuwien.ac.at (W.W.); bloeschl@hydro.tuwien.ac.at (G.B.)

² Department of Geodesy and Geoinformation, TU Wien, 1040 Vienna, Austria;

mariette.vreugdenhil@geo.tuwien.ac.at (M.V.); sebastian.hahn@geo.tuwien.ac.at (S.H.)

³ Institute for Land and Water Management Research, Federal Agency for Water Management Austria, 3252 Petzenkirchen, Austria; peter.strauss@baw.at

* Correspondence: isabella.pfeil@geo.tuwien.ac.at

Received: 24 September 2018; Accepted: 7 November 2018; Published: 11 November 2018



Abstract: Previous validation studies have demonstrated the accuracy of the Metop-A ASCAT soil moisture (SM) product, although over- and underestimation during different seasons of the year suggest a need for improving the retrieval algorithm. In this study, we analyzed whether adapting the vegetation characterization based on global parameters to regional conditions improves the seasonal representation of SM and vegetation optical depth (τ). SM and τ are retrieved from ASCAT using both a seasonal (mean climatological) and a dynamic vegetation characterization that allows for year-to-year changes. The retrieved SM and τ are compared with in situ and satellite SM, and with vegetation products (SMAP, AMSR2, and SPOT-VGT/PROBA-V). The study region is set in an agricultural area of Lower Austria that is characterized by heterogeneous land cover and topography, and features an experimental catchment equipped with a SM network (HOAL SoilNet). We found that a stronger vegetation correction within the SM retrieval improves the SM product considerably (increase of the Spearman correlation coefficient r_s by 0.15 on average, and r_s comparable to SMAP and AMSR2). The vegetation product derived with a dynamic vegetation characterization compares well to the reference datasets and reflects vegetation dynamics such as start and peak of season and harvest. Although some vegetation effects cannot be corrected by the adapted vegetation characterization, our results demonstrate the benefits of a parameterization optimized for regional conditions in this temperate climate zone.

Keywords: microwave remote sensing; advanced scatterometer (ASCAT); soil moisture; vegetation optical depth

1. Introduction

Soil moisture (SM) plays an important role in the water and carbon cycle and needs to be considered in a number of related applications. SM datasets are used in hydrological model calibration and runoff predictions [1–3], irrigation scheduling [4,5], rainfall estimation [6,7], drought monitoring [8–10], modeling of groundwater depletion [11], and vegetation and crop growth monitoring [12], amongst many others. These applications require accurate and readily available datasets on different scales.

Over the past 30 years, remote sensing missions have emerged that observe global SM conditions from space [13]. The Soil Moisture Ocean Salinity (SMOS) [14] and Soil Moisture Active Passive

(SMAP) [15] missions are dedicated SM missions operating in L-band, providing global passive SM observations. Another sensor that can be used for the retrieval of global SM, though not designed for this purpose, is the Advanced Microwave Scanning Radiometer 2 (AMSR2), a passive multi-frequency instrument on board GCOM-W1 [16]. An active C-band sensor suitable for SM retrieval is the Advanced Scatterometer (ASCAT) on board the Metop satellites.

At the Vienna University of Technology (TU Wien), a change detection algorithm has been developed to retrieve SM from the scatterometers on board the European remote sensing satellites (ERS) [17], which was later adapted and improved for ASCAT [18]. Many studies have evaluated the ASCAT SM product over different regions. High correlations between ASCAT and in situ data have been observed in the Bibeschbach catchment in Luxembourg [19], in southwestern France [20] and for selected networks across Europe [21]. However, weaknesses in the representation of the seasonal cycle in ASCAT SM have been described: Wagner et al. [22] observed ASCAT SM values in the summer months that are consistently higher than SM values from SMOS and in situ stations in two watersheds in the United States. Three possible reasons were discussed which can lead to high SM in these catchments: Under very dry conditions, sub-surface scattering can increase the backscatter, and consequently the derived SM [12,23]. On the other hand, wet soil surfaces and wetlands can also lead to enhanced backscatter. A third possible reason is a too weak vegetation correction. Barbu et al. [24] found that, over France, temporal correlations between the satellite data and modeled SM increase by 0.07–0.09 when applying a seasonal correction to the SM values instead of a bias correction that is static throughout the year. This is due to low ASCAT SM values in May, which are adjusted by the seasonal correction.

The TU Wien SM model uses the multi-angle viewing capacity of the ASCAT sensor to correct for vegetation [25]. It has been shown that the vegetation characterization can be converted into vegetation optical depth (τ_a) [26], which is an indicator of the vegetation water content, both the leaf and woody components of the total above-ground biomass [27]. Similar to SM, vegetation is an important variable in the water and carbon cycle. It has been shown that τ from microwave remote sensing is suitable for continuously monitoring vegetation dynamics [27,28], and complements datasets from optical satellites such as the normalized difference vegetation index (NDVI) and leaf area index (LAI) [27].

The aim of this study was to improve both the ASCAT SM and τ retrievals by optimizing model parameters linked to the vegetation characterization. The representation of the seasonal cycle in the ASCAT SM and τ datasets is assessed against SM and τ from different satellite and in situ datasets. Since the seasonal bias was observed in temperate climate regions, a region in Lower Austria was chosen as a representative area for this analysis. Since 2013, an in situ SM network is operated in an agricultural catchment in this area. Section 2 gives an overview of the study area, followed by a description of datasets in Section 3. The applied methods are described in Section 4. Section 5 describes the results of the study for SM and τ , which are discussed in Section 6.

2. Study Site

The study site is situated in Petzenkirchen, Lower Austria (Figure 1). A Hydrological Open Air Laboratory (HOAL) is operated in an agricultural catchment, providing extensive field data used for investigating catchment evapotranspiration, runoff processes, sediment transport, nutrient dynamics, contaminant pathways and spatial patterns in SM [29]. The area is characterized by a humid climate with higher precipitation in summer than in winter. From 1990 to 2014, a mean annual temperature of 9.5 °C and a mean annual rainfall of 823 mm year^{−1} have been observed. Eighty-seven percent of the total area of the HOAL is arable land; the remaining parts are forests (6%), pasture (5%) and paved areas (2%). Two main crop growing seasons are found in the HOAL: winter crops such as wheat, barley and rapeseed are usually planted in autumn and harvested in July. Summer crops (in the HOAL mainly corn) are usually planted in April and harvested in September/October. Between the harvest and seeding of the main crops, green fertilizers are often planted on the fields. Depending on the weather, seeding and harvest dates can vary by a few weeks from year to year. The HOAL catchment is

classified as “Cropland, rainfed” by the ESA CCI land cover dataset [30], but it also features evergreen and deciduous forests and grasslands.

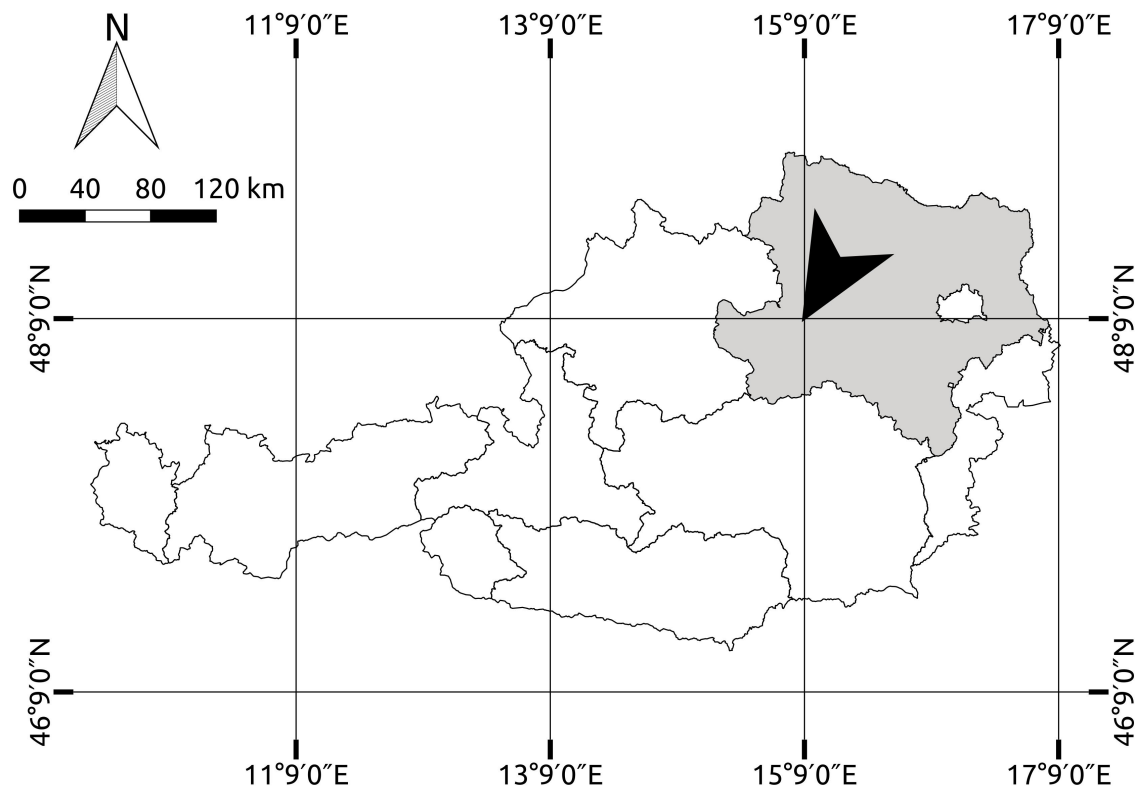


Figure 1. Location of the Hydrological Open Air Laboratory (HOAL) in Lower Austria.

Figure 2 (left) shows the area that is (approximately) covered by the ASCAT, AMSR2 and SMAP 3-dB footprints. This area is considerably larger than the catchment, but has similar topographic conditions and land cover as the HOAL. The ESA CCI land cover dataset for the ASCAT, SMAP and AMSR2 footprints is shown in Figure 3. The dominant land cover classes found in the study area are rainfed cropland, evergreen needle leaf and deciduous broad leaf forest as well as grasslands. More details about the study area are listed in Table 1.

Table 1. Study area characteristics.

	HOAL	Sensor Footprints
Location (center)	48°9'N 15°9'E	approx. 48°9'N 15°9'E
Extent	66 ha	490–1800 km ²
Elevation	268–323 m a.s.l.	200–900 m a.s.l.
Mean slope	8%	8.5%
Arable land	87%	approx. 60%
SM stations	31	

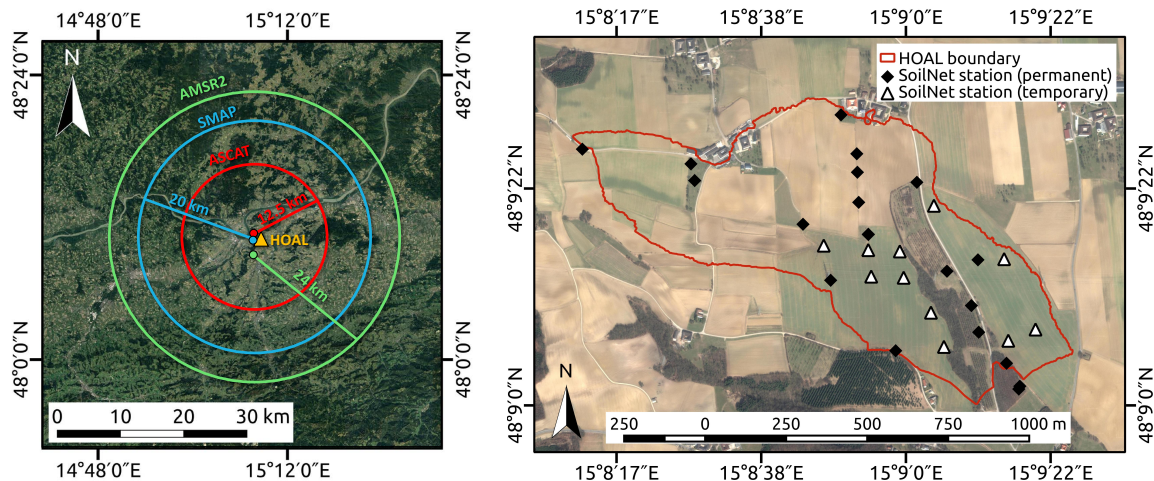


Figure 2. Schematic overview of the 3-dB sensor footprints of ASCAT, SMAP and AMSR2 (left); and distribution of permanent and temporary stations in the HOAL catchment (right). Map data ©2018 Google.

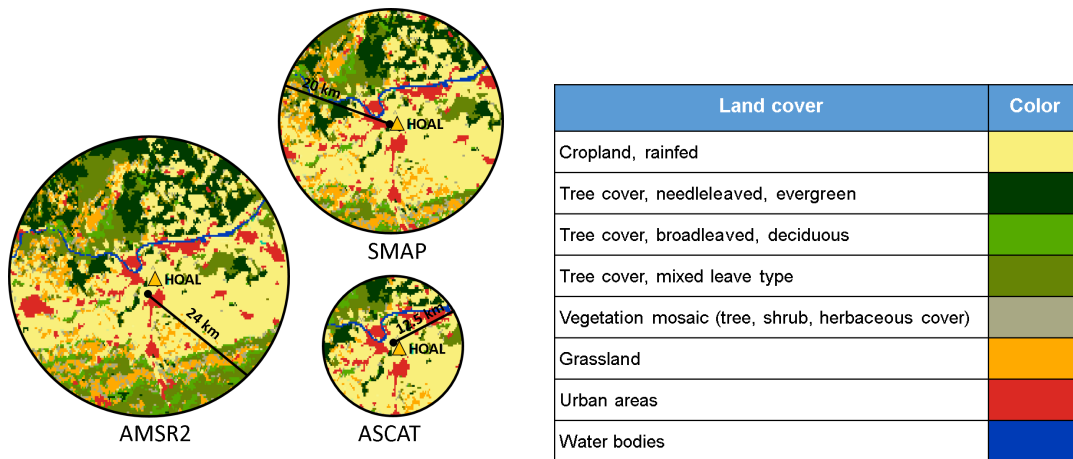


Figure 3. ESA CCI land cover in the 3-dB sensor footprints of ASCAT, SMAP and AMSR2.

3. Datasets

3.1. In Situ Soil Moisture

Since 2013, an in situ SM network has been operated in the Hydrological Open Air Laboratory (HOAL), which measures SM at different depths (5, 10, 20, and 50 cm) every 30 min using the Time Domain Transmission (TDT) method. Twenty permanent stations are installed at selected locations that represent the different hydrologic conditions and land cover types present in the catchment. Additionally, 11 stations are installed temporarily inside agricultural fields, which are removed during farmers' field management practices (planting, harvesting, ploughing, etc.). For this study, the time series of the upper sensors (5 cm) of the in situ stations, averaged over the entire catchment, are used. The network is in the following referred to as HOAL SoilNet. Figure 2 (right) shows the distribution of the permanent and temporary SM stations in the catchment.

3.2. Satellite Data

3.2.1. ASCAT

Backscatter measurements from the ASCAT sensor on board Metop-A are available since January 2007 and used to retrieve SM and τ_a with the TU Wien model [17,18,25,26]. A schematic overview of the semi-empirical TU Wien modeling scheme is provided in Figure 4 (top).

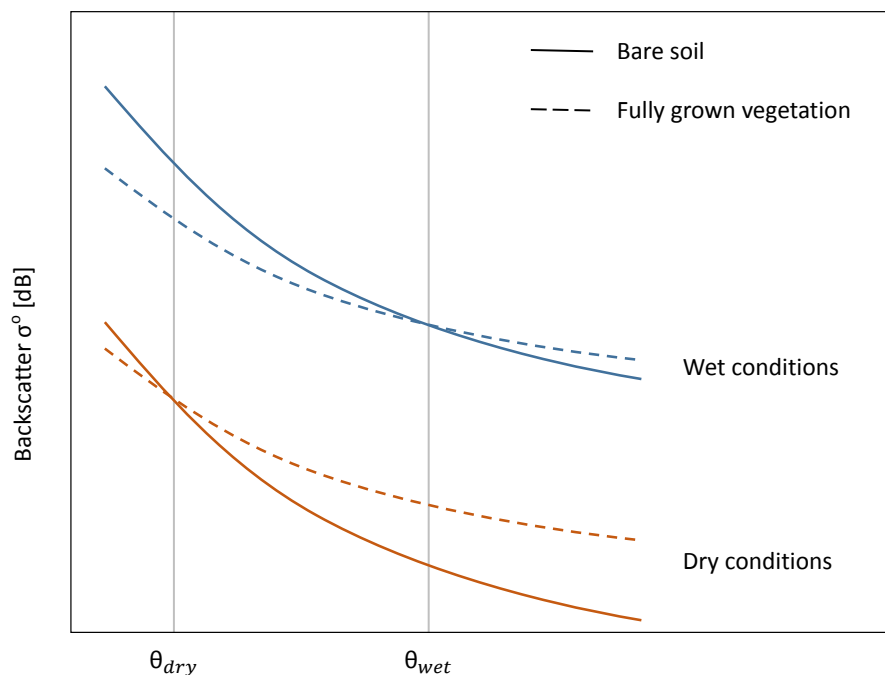
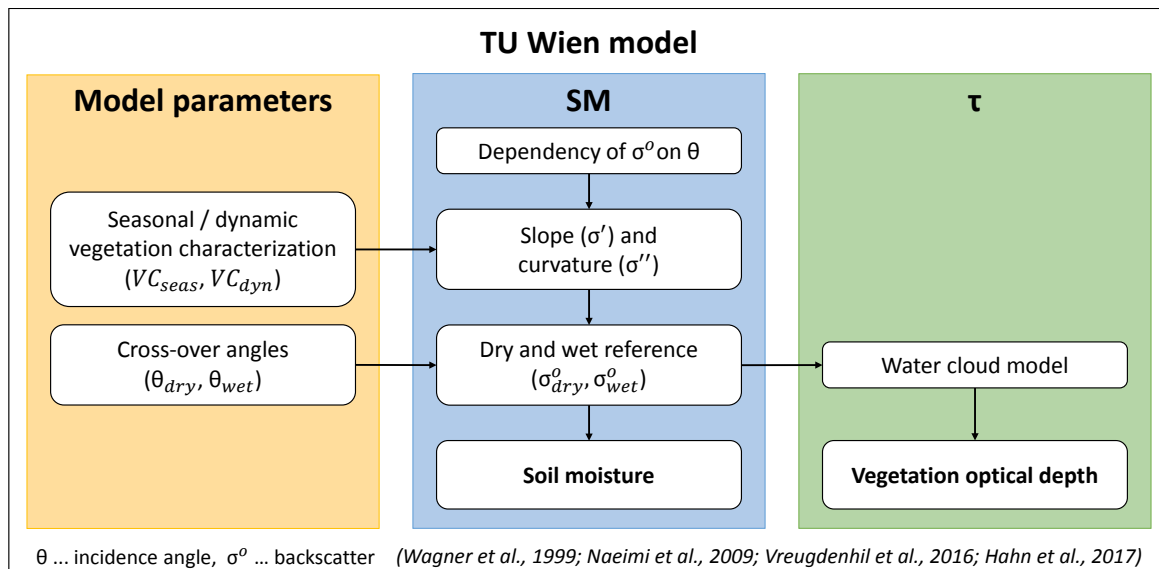


Figure 4. Main steps of the TU Wien algorithm for the retrieval of SM and τ (**top**); and dependency of backscatter (σ°) on incidence angle θ , soil moisture and vegetation (**bottom**); after [12].

The observed backscattering coefficient σ° is assumed to depend only on the incidence angle (θ), degree of saturation (Θ_s), and vegetation cover (V). Wagner et al. [31] found that both a change in Θ_s and in V lead to an increased σ° , and that the effect of V is typically more pronounced at high incidence angles (Figure 4, bottom panel). At two incidence angles, seasonal vegetation changes are assumed to not affect the observed σ° ; those are the so-called dry and wet cross-over angles (θ_{dry} and θ_{wet}), which were empirically set to 25° and 40° globally [18]. The incidence angle dependency of σ° is described by a second-order Taylor polynomial in the TU Wien model. The first and second derivatives of the σ° – θ –relationship are referred to as slope (σ') and curvature (σ''). Those can be used to estimate the backscatter at any arbitrary incidence angle [25]. In the TU Wien model, backscatter observations are normalized to a reference incidence angle of 40° to remove the incidence angle dependency [31]; this backscatter time series is termed σ_{40}° .

At θ_{dry} and θ_{wet} , where, as mentioned above, the observed backscatter is assumed to be independent of V , the lowest and highest 10% of backscatter measurements are estimated and averaged to obtain the historically “driest” and “wettest” backscatter values. These two values are then transferred back to the reference incidence angle of 40° using σ' and σ'' . Due to σ' and σ'' varying from day to day, time series instead of single values for the driest and wettest backscatter values are obtained. These time series are termed the dry and wet references (σ_{dry}° and σ_{wet}°). They describe the effects of different static and dynamic parameters (e.g., soil roughness, soil texture, and V) on the backscatter observations. Since soil roughness and soil texture are assumed to be static over the retrieval period, dynamics in σ_{dry}° and σ_{wet}° are an indicator of the vegetation state [32]. The difference between σ_{wet}° and σ_{dry}° , also called the sensitivity, determines the dynamic range of the retrieved SM dataset. A small difference leads to a low dynamic range and consequently higher noise in the retrieval [18].

In a final step of the TU Wien model, σ_{40}° is scaled between σ_{dry}° and σ_{wet}° to obtain a SM time series that is corrected for the effect of vegetation (see Equation (1)).

$$\Theta_s = \frac{\sigma_{40}^\circ - \sigma_{dry}^\circ}{\sigma_{wet}^\circ - \sigma_{dry}^\circ} \quad (1)$$

ASCAT τ (hereafter referred to as τ_a) is derived from σ_{dry}° and σ_{wet}° using a water cloud model [26]. SM and τ_a are retrieved at a spatial resolution of 25 km for every 1–3 days and sampled on a discrete global grid with regular 12.5 km point spacing within the TU Wien model [17,18,26].

Traditionally, the vegetation state is modeled using seasonal parameters, i.e., one value for each day of the year, and not accounting for year-to-year variations in the vegetation cycle (referred to as seasonal vegetation characterization VC_{seas}). In times of limited backscatter data availability, e.g., the scatterometers on board ERS-1 and ERS-2 (ESCAT), this was necessary to obtain robust estimates of the incidence angle dependency of the observed backscatter. Since the operation of the ASCAT sensor, which has a much higher temporal revisit rate than its predecessor ESCAT, this is no longer necessary. Melzer [33] introduced a Kernel smoother in order to obtain dynamic parameters not only for each day of the year, but for all years individually. This is referred to as dynamic characterization (VC_{dyn}) in the following. Hahn et al. [25] showed the robustness of the dynamic characterization globally and Vreugdenhil et al. [34] showed its sensitivity to inter-annual vegetation dynamics over Australia.

3.2.2. AMSR2

The passive radiometer AMSR2 on-board GCOM-W1 was launched by the Japan Aerospace Exploration Agency (JAXA) in 2012. Similar to its predecessor AMSR-E (Advanced Microwave Scanning Radiometer on the Earth Observing System), it observes brightness temperature at C- and X-band. In this study, SM and τ derived with the Land Parameter Retrieval Model (LPRM) algorithm (version LPRMv05) [16,35] were selected as reference datasets. To be comparable to the ASCAT datasets, only C-band observations are used in this study. The AMSR2 datasets are provided daily at a spatial resolution of $62 \text{ km} \times 35 \text{ km}$ (C-band).

Kim et al. [36] compared AMSR2 SM derived with the LPRM algorithm to field measurements from COSMOS stations over the USA and found consistent temporal patterns of the two datasets, although AMSR2 tended to overestimate SM [37]. Cho et al. [38] showed AMSR2 to provide a valuable successor to the AMSR-E mission in Australia. More on the validation of the LPRM AMSR2 SM product can be found, e.g., in [39–41]. To the authors' knowledge, only a brief comparison of the LPRM AMSR2 τ (later referred to as τ_{a2}) to other τ products has been carried out by Cui et al. [42]; τ derived from AMSR-E using the LPRM algorithm has however been evaluated against the widely used NDVI [27], applied in agricultural drought monitoring studies [43] and validated in the Sahel [28]. Furthermore, it has been applied to the monitoring of global change in the total above ground vegetation water content and biomass over various ecosystems and to the attribution of observed changes to environmental and human drivers [44].

3.2.3. SMAP

The SMAP L-band radiometer measures brightness temperature with a revisit time of 1–3 days globally at a spatial resolution of approximately 40 km [15]. The SM product is derived by inverting a τ - ω -model [45,46]. Here, the SMAP L3 passive product, version V004, has been selected for a comparison with ASCAT datasets, which is available from 2015 onward. Since SMAP operates in L-band, it is assumed to penetrate deeper into the vegetation than higher frequency bands, and is less affected by radio frequency interference (RFI) [47].

A validation of the SMAP SM products was carried out by Colliander et al. [48], who found that, over 18 core validation sites, the passive product meets the target unbiased root mean square error of 0.04 m³/m³ volumetric SM. A comprehensive assessment of the performance of the passive SM product can be found in [49]. The SMAP V004 product includes estimates of vegetation water content (VWC), which is a combined estimate from NDVI (canopy water content) and past field observations and LAI (stem water content) [50]. For the comparison with τ from ASCAT and AMSR2, SMAP vegetation opacity (VO; later referred to as τ_s) is used, which is equivalent to the VWC product multiplied by a constant scaling factor. To the authors' best knowledge, the τ_s product has so far only been evaluated by Cui et al. [42]; however, an alternate approach for the retrieval of τ from SMAP observations using the multi-temporal dual channel algorithm has been applied and evaluated by Konings et al. [47].

3.2.4. SPOT-VGT and PROBA-V

SPOT-VGT (1999–May 2014) and its successor PROBA-V (June 2014–ongoing) are global vegetation monitoring missions operating in the optical domain [51]. In this study, leaf area index (LAI) from the satellites is included as a reference for the evaluation of τ_a . The CCI land cover dataset [30] is used to classify the SPOT-VGT/PROBA-V pixels and to obtain LAI time series for croplands, forests and grasslands.

3.3. Pre-Processing

In situ measurements from 20 permanent and 11 temporary sensors installed at 5 cm depth are averaged to a mean in situ SM time series. Frozen conditions and surface snow are masked using average Layer 1 soil temperature (0.00–0.10 m), average surface temperature and snow water equivalent data from the global land data assimilation system (GLDAS; version 2.1) [52]. The same masking is applied to the satellite datasets. The soil penetration depth of active C-band systems such as ASCAT ranges from 0.5 and 2 cm under normal, not too dry conditions; passive systems observe the brightness temperature emissions which originate from the top 0–2 cm (e.g., C-band sensor AMSR2) to 3–5 cm of the soil (e.g., L-band sensor SMAP) [15,18,53]. To make the satellite and in situ datasets comparable, a soil water index (SWI) [54] with a small time scale parameter (T value of two days) is applied to all satellite SM time series. Thus, the satellite SM values better comply with the measurement depths of the HOAL SoilNet stations (5 cm).

4. Methods

Over- or underestimation of SM during spring or summer are likely to be caused by an insufficient correction of vegetation effects on the backscattered signal. The vegetation correction applied in the TU Wien SM retrieval algorithm depends on two components: the choice of cross-over angles and the use of a seasonal or dynamic vegetation characterization. Similar to the vegetation correction needed for the retrieval of SM, τ_a is derived from the dry and wet references. Thus, an improvement of the vegetation characterization should lead to an improvement of both the SM and τ_a datasets. Figure 5 shows σ_{dry}° and σ_{wet}° for two selected pairs of incidence angles (10°/30° and 25°/40°) and both VC_{seas} (top) and VC_{dyn} (middle). Metop-A ASCAT backscatter is displayed after its normalization to

an incidence angle of 40° (σ_{40}°). To enable a comparison of the time series with meteorological data, air temperature and rainfall and snowfall rates from GLDAS are displayed (bottom).

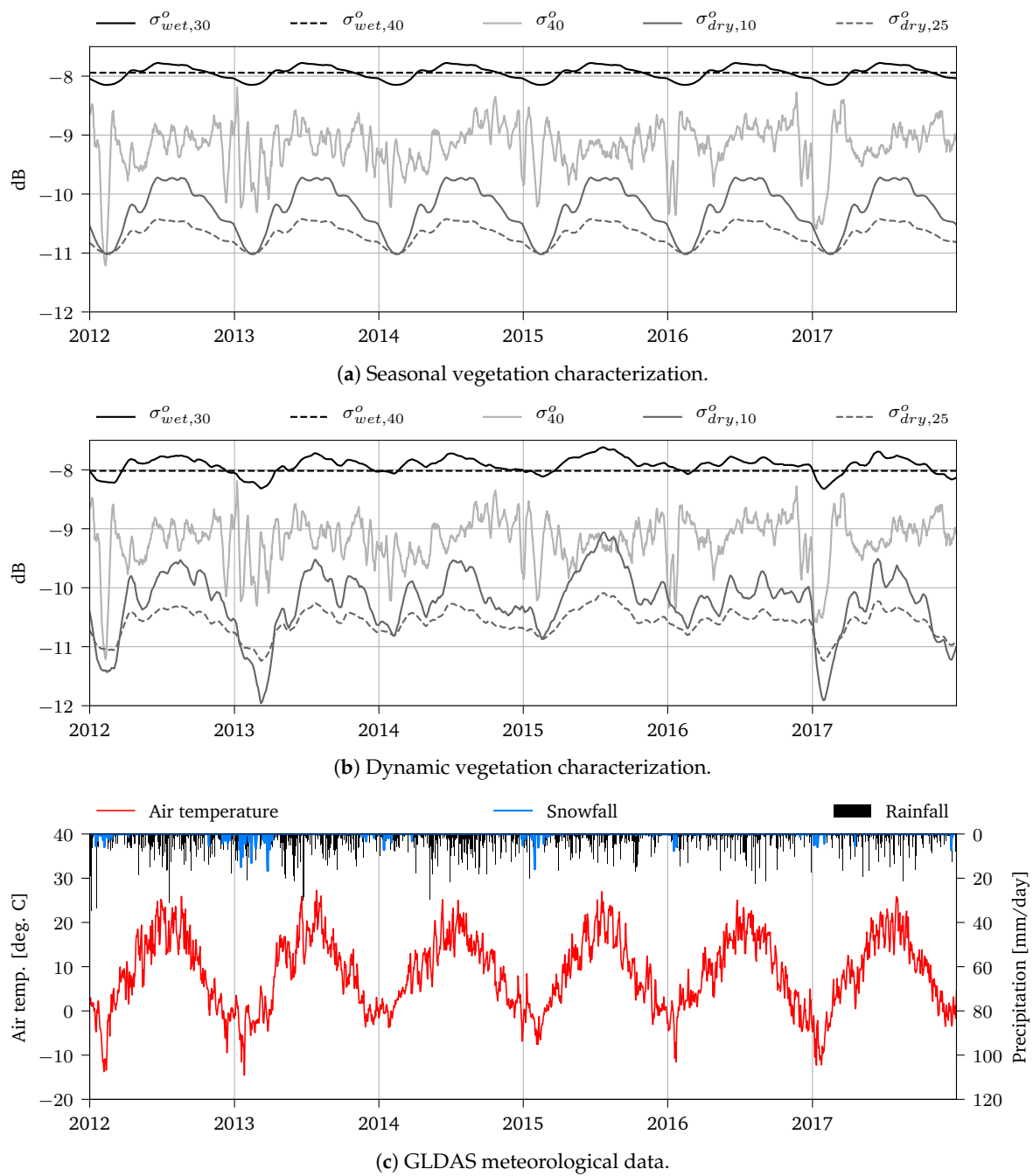


Figure 5. Dry and wet reference derived from Metop-A ASCAT using two different pairs of cross-over angles ($10^\circ/30^\circ$ and $25^\circ/40^\circ$) and seasonal (a) and dynamic vegetation characterization (b). Additionally, the backscatter normalized to an incidence angle of 40° (σ_{40}°) is displayed. (c) GLDAS air temperature, rainfall rate and snowfall rate for the study region.

4.1. Type of Vegetation Characterization

Originally, and in the latest released ASCAT SM product (H111), yearly climatologies are used for correction, i.e., every day of the year undergoes the same correction each year (seasonal vegetation correction, VC_{seas} ; Figure 5a). The approach presented by Melzer [33], Vreugdenhil et al. [26] and Hahn et al. [25] included inter-annual variations in the vegetation dynamics (VC_{dyn} ; Figure 5b). In this study, the effect of applying VC_{dyn} instead of VC_{seas} was analyzed.

4.2. Selection of Cross-Over Angles

Due to the transferring of the driest and wettest observed values from θ_{dry} and θ_{wet} back to the reference incidence angle of 40° , the amplitude of the vegetation characterization is determined by the choice of the dry and wet cross-over angles; lower cross-over angles lead to a larger amplitude of the vegetation characterization, i.e., the model assumes a stronger effect of vegetation (Figure 5). In the following, this is referred to as a stronger vegetation characterization. Wagner [55] found that the cross-over angle of dry surfaces is lower than for wet surfaces. Globally, the cross-over angles are set to the empirically determined values of 25° (dry soil) and 40° (wet soil; compare Figure 4, bottom) [18]. To optimize the retrieval to regional conditions, the effect of modifying the cross-over angles was analyzed in this study.

4.3. Evaluation of the Results

The effect of changing the cross-over angles and selecting VC_{seas} or VC_{dyn} was analyzed for both SM (Section 5.1) and τ (Section 5.2). For SM, HOAL in situ data were used as a reference, as well as SM from AMSR2 and SMAP. ASCAT τ (τ_a) was compared to τ from AMSR2 (τ_{a2}) and SMAP (τ_s) as well as to LAI retrieved from SPOT-VGT/PROBA-V observations.

For SM, the evaluation was based on the Spearman and Pearson correlation coefficients (r_s and r_p) as well as on the unbiased root-mean-square deviation ($ubRMSD$). In the case of τ , the focus is given to the visual interpretation of the time series, since high r values are mainly associated with smooth τ curves that approximate the mean yearly cycle, but do not necessarily contain interesting features coming from different crop types (see Section 5.2). As a reference for the visual interpretation, photos of the HOAL catchment, information on the crop types, planting and harvesting dates as well as meteorological data (see Figure 5c) were used.

Although the analyzed spatial scales are considerably different (local in situ network vs. sensor footprints of multiple km^2), we consider the HOAL catchment appropriate for the comparison with satellite data due to the similar land cover types and topographic conditions described in Section 2.

5. Results

5.1. Soil Moisture

In the following, retrievals of ASCAT SM using different settings for the above described parameters are compared to satellite and in situ SM.

5.1.1. Cross-Over Angle Optimization

Figure 6 shows r_s between different versions of ASCAT SM and the reference datasets. r_s was calculated for the available period of the respective datasets: 2015–2017 for SMAP, 2012–2017 for AMSR2, and 2013–2017 for the in situ data from the HOAL catchment. For all datasets and for both VC_{seas} and VC_{dyn} , higher correlation coefficients (up to 0.8) are obtained with a stronger vegetation correction, i.e., lower cross-over angles than the original pair of 25°/40°. Only when comparing with SMAP, r_s increases with increasing cross-over angles when correlating it with dynamically corrected ASCAT SM (Figure 6b). All correlations are highly significant ($p < 0.01$).

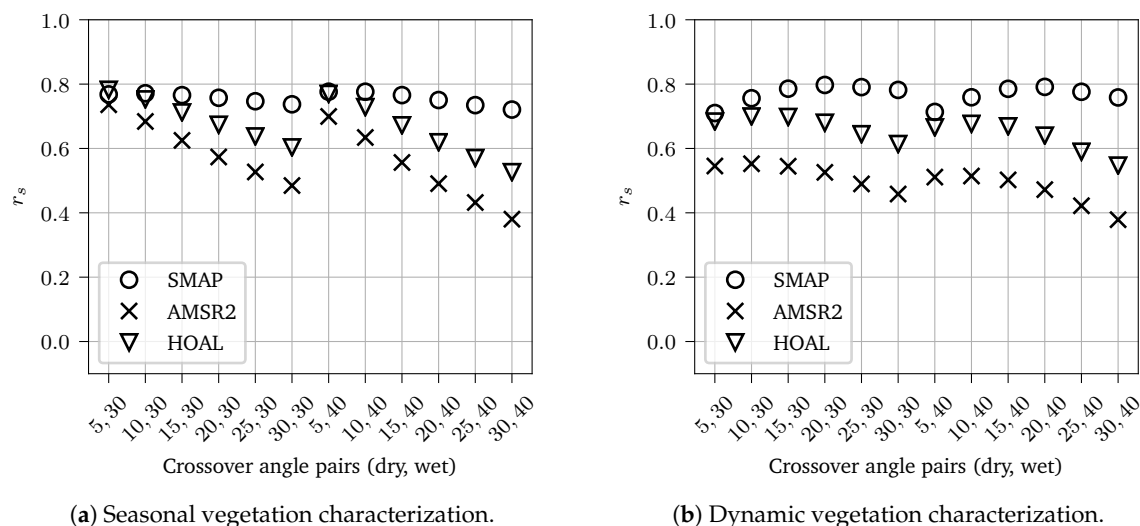


Figure 6. Spearman correlation coefficient (r_s) between different retrievals of ASCAT SM and SMAP (circles), AMSR2 (crosses) and HOAL in situ SM (triangles) for 2012–2017. ASCAT SM was retrieved using: (a) VC_{seas} ; and (b) VC_{dyn} .

The sensitivity to SM was determined by the selection of cross-over angles. In general, lower cross-over angles ($\theta_{dry} = 5^\circ$ – 15° , $\theta_{wet} = 30^\circ$) lead to a lower dynamic range between σ_{dry}° and σ_{wet}° , because it is expected that vegetation has a stronger effect on the overall backscatter intensity. However, this leads to a higher noise in the SM retrieval, because the dynamic range of σ_{dry}° and σ_{wet}° defines how sensitive the (remaining) backscatter signal is to changes in soil moisture. Furthermore, low cross-over angles can create more backscatter outliers ($\sigma_{40}^\circ < \sigma_{dry}^\circ$ and $\sigma_{40}^\circ > \sigma_{wet}^\circ$), which are typically corrected to 0% ($-25\% > SM < 0\%$) and 100% ($100\% > SM < 125\%$). However, extreme outliers (i.e., $SM < -25\%$ or $SM > 125\%$) are marked as invalid SM estimates and therefore set to NaN. Due to these characteristics of the algorithm, the cross-over angle pair of 10° and 30° is considered the optimal choice for the study region, although other cross-over angle pairs lead to higher correlation coefficients (Figure 6). In the following, all results are shown for the original and optimized cross-over angles pairs of 25°/40° and 10°/30°.

5.1.2. Quantitative Comparison

As stated by Wagner et al. [12], validation results of different types of datasets should also be interpreted in a relative context, for example by comparing different satellite datasets with the same in situ dataset. Therefore, r_s and r_p as well as the $ubRMSD$ were calculated between each of the satellite datasets and the HOAL SoilNet time series (Figure 7). For each satellite–in situ pair, the time period for which both datasets are available was used; the time periods are limited by the availability of HOAL SoilNet data (from August 2013 onward) and SMAP data (from April 2015 onward). SMAP and AMSR2 show r_s and r_p of 0.77 and 0.78 (SMAP) and 0.71 and 0.69 (AMSR2) with the in situ data. For the respective periods, ASCAT and in situ SM show correlations ranging from 0.57 to 0.75, with higher correlation coefficients clearly associated with a stronger vegetation correction (lower cross-over

angles). The $ubRMSD$ between SMAP and AMSR2 and the in situ data is 0.034 and 0.038, and ranges from 0.036 to 0.048 for the different ASCAT datasets. Using cross-over angles of 10° and 30° leads to ASCAT datasets that have a smaller $ubRMSD$ and that are more similar to SMAP and AMSR2. Figure 7 also shows that the usage of VC_{seas} or VC_{dyn} has a smaller effect on the metrics than the choice of cross-over angle pair. These results show that in the current SM product, the cross-over angles are not optimal and the applied vegetation correction thus not ideal for the study area.

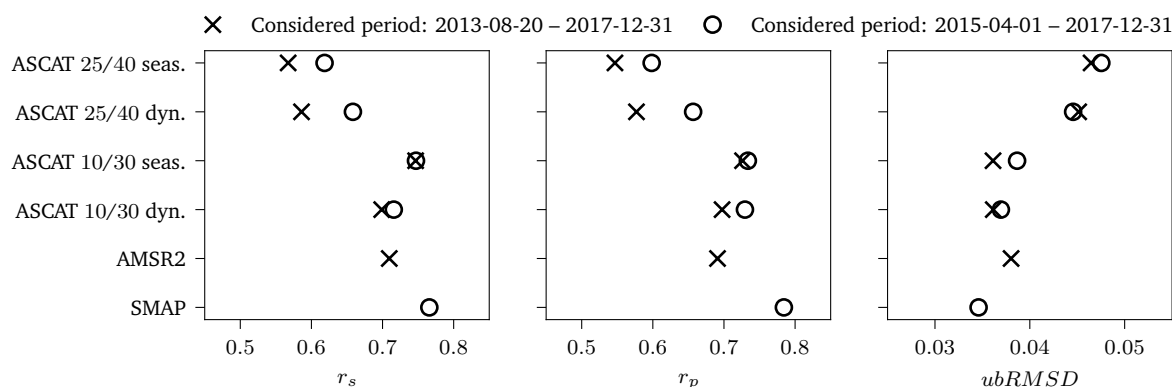


Figure 7. Spearman and Pearson correlation coefficients (r_s and r_p) and $ubRMSD$ between HOAL in situ SM and different satellite SM datasets. The metrics have been calculated for 20 August 2013 (limited by availability of HOAL SoilNet data) and 1 April 2015 (limited by availability of SMAP data) until the end of 2017.

In a next step, r_s has been calculated between the in situ and satellite datasets for different seasons (spring: March–June; summer: July–September; and autumn and winter: October–February). Figure 8 shows r_s and the change obtained from using different cross-over angle pairs. In the spring months, r_s between ASCAT and HOAL increases by 0.16 (VC_{seas}) and 0.12 (VC_{dyn}) when using lower cross-over angles, i.e., a stronger vegetation correction. In summer, only little (VC_{seas}) or even negative changes (VC_{dyn}) are achieved; in autumn, both a stronger VC_{seas} and VC_{dyn} improve ASCAT with respect to the HOAL SoilNet (+0.18 and +0.09, respectively). Over the entire period, the change of r_s is positive (+0.15 on average) when applying a stronger vegetation correction, and the HOAL–ASCAT r_s becomes comparable to the HOAL–AMSR2 and HOAL–SMAP r_s . Whether the correlation improves or deteriorates in different seasons probably depends on several reasons. r_s has been calculated over up to six years, all of which experienced different weather conditions. When looking at individual years, larger improvements are made in 2015 and 2017 (rather dry years) than in 2014 and 2016 (rather wet); in 2014 and 2016, r_s also increases, but is significantly higher when using VC_{seas} (not shown). Such differences between the years are also observed in the τ_a time series (see Section 5.2). A possible reason could be different temperature and rainfall conditions, leading to differences in the vegetation growth that are not sufficiently represented by the vegetation correction.

5.1.3. Qualitative Comparison

Finally, we examined the time series obtained from different model parameters (Figure 9; a moving mean with a 14-day window has been applied on all datasets for better readability). In this figure, it can be seen that, in all years, a stronger vegetation correction for the SM retrieval (blue solid line) leads to a seasonal representation of SM in spring and summer that is closer to the reference datasets, compared to the original SM product (dotted black line). However, not the entire effect is corrected this way; ASCAT SM is still—in some years (e.g., 2014) considerably—lower in spring than the other datasets. This will be further discussed in Section 6.

Apart from the mostly positive effect on the seasonal representation, we observe a negative side effect that can occur in years with high vegetation activity. In the study area, 2015 was a very warm and dry year. When choosing VC_{dyn} and cross-over angles of 10° and 30° , the effect of the vegetation correction may be so strong during summer that no SM can be retrieved anymore, leading to a data gap (see Figure 9b, solid black line in July–August 2015; also visible in Figure 5b).

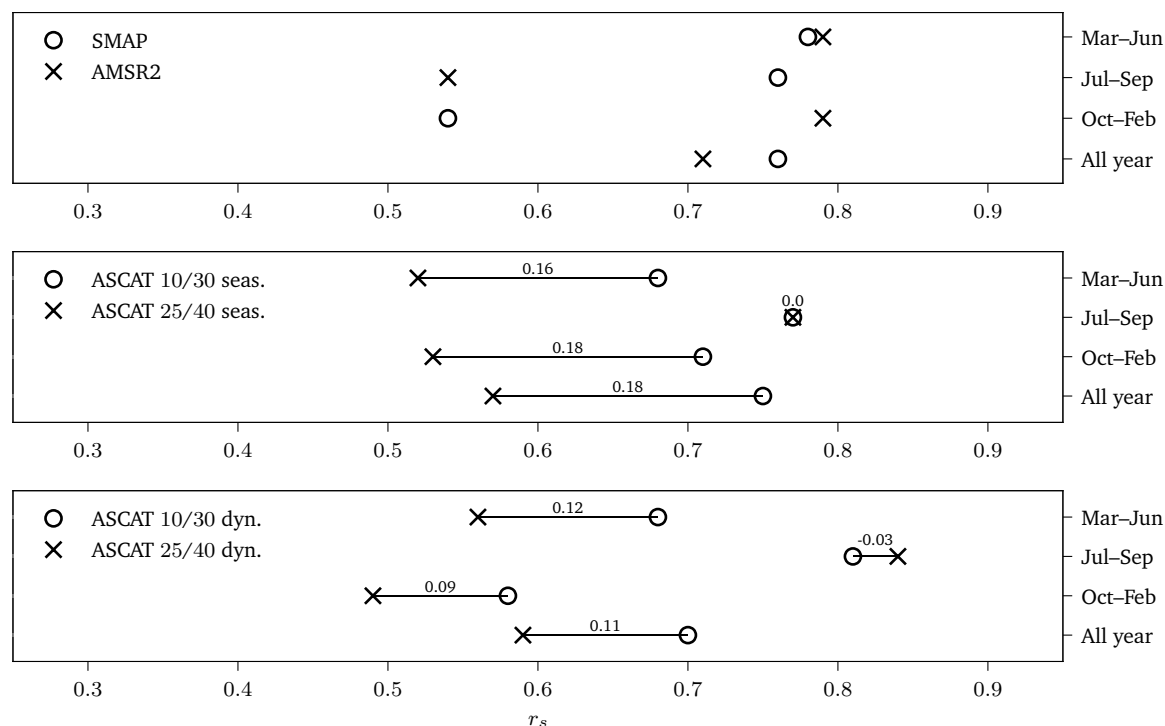
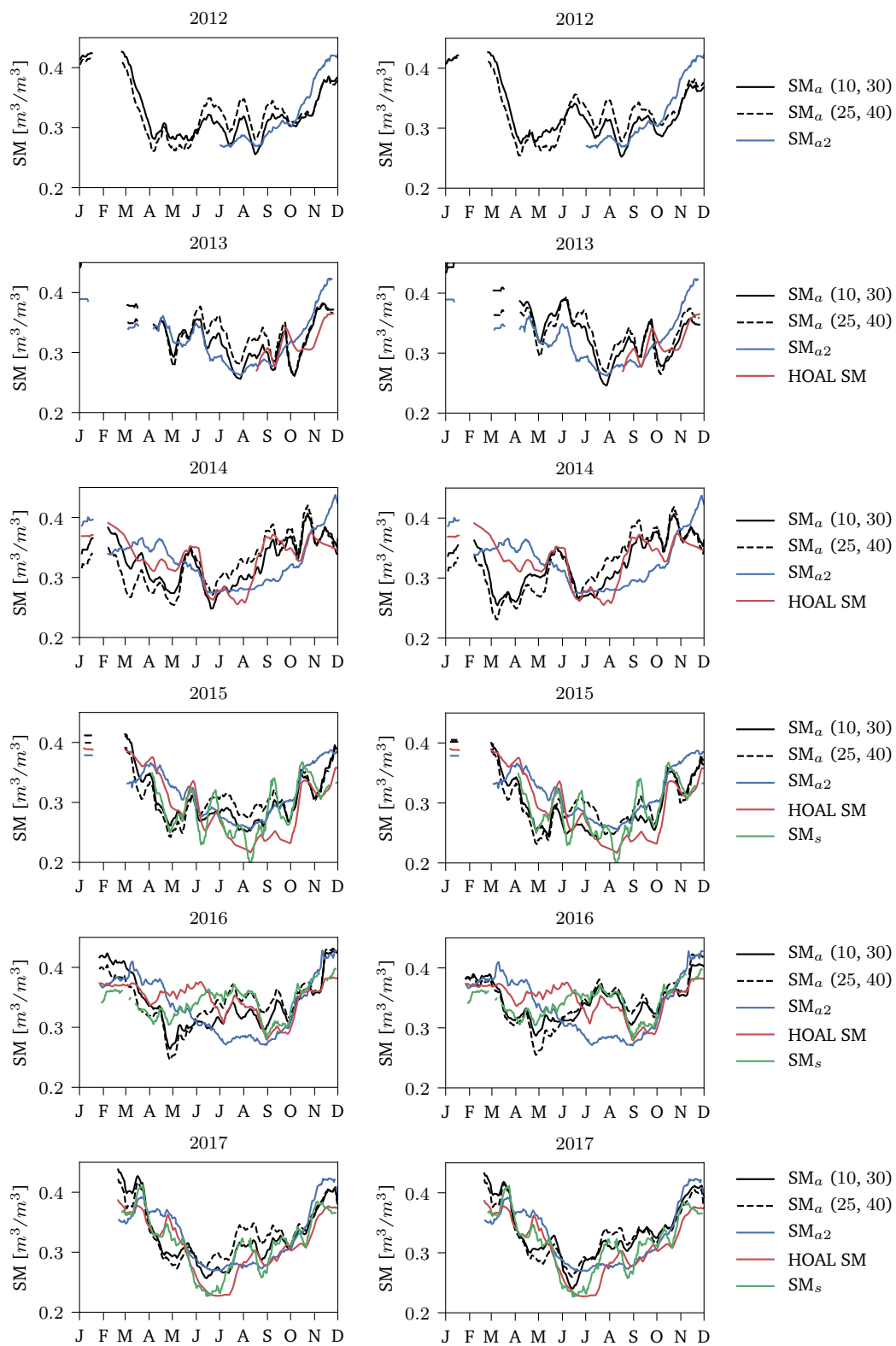


Figure 8. Spearman correlation coefficient (r_s) between HOAL in situ SM and different satellite SM datasets for different seasons.

Another issue to be considered are the penetration depths of the C- and L-band sensors (upper few centimeters of the soil), compared to the installation depth of the in situ sensors (5 cm, i.e., deeper than satellite sensors penetrate under normal, not extremely dry conditions). Although this discrepancy is reduced by the application of the SWI with a T value of two days, there can still be effects such as a faster drying out of the soil that is only seen by satellites but not measured by the deeper in situ sensors. Consequently, lower SM values observed by satellite sensors do not necessarily mean erroneous retrievals, but can simply be caused by different reference depths.

5.2. Vegetation Optical Depth (τ)

To evaluate the performance of τ_a in the study area, it is compared to τ_s and τ_{a2} , and LAI from SPOT-VGT/PROVA-V, resampled to the ASCAT footprint.



(a) Seasonal vegetation characterization.

(b) Dynamic vegetation characterization.

Figure 9. SM from ASCAT (SM_a), AMSR2 (SM_{a2}), SMAP (SM_s) and the in situ network (HOAL SM) for the years 2012 to 2017; SM_a retrieved using: (a) VC_{seas} ; and (b) VC_{dyn} . A moving mean (window: 14 days) has been applied to all datasets for better readability.

5.2.1. Quantitative Comparison

In a first step, linear regressions of LAI and satellite τ datasets have been calculated (Figure 10). The steeper slopes (0.04–0.05) observed with τ_{a2} and τ_s (right column) are in line with the findings of Lawrence et al. [56], who observed a slope of 0.05 between MODIS LAI and τ from SMOS. The slope of τ_a and LAI is smaller, whereas larger slopes (0.02) for τ_a are obtained when applying a VC_{seas} (left column). Using a VC_{dyn} (middle column) leads to smaller slopes and more outliers, especially when applying a stronger vegetation characterization. A r_s of 0.79 and 0.75 is observed for τ time series with small amplitudes and no inter-annual variation (τ_s , and τ_a derived with a VC_{seas}). If inter-annual variations are included in a product, r_s decreases significantly to values ranging from 0.29 to 0.55 (τ from AMSR2 and τ_a derived with a VC_{dyn}), but corresponds to correlation values found by Jones et al. [57] between MODIS LAI and τ from AMSR-E in temperate climates. R^2 and r_s suggest that VC_{dyn} does not add value, but deteriorates the τ_a product. However, effects caused by sensitivities to different vegetation characteristics of optical and microwave sensors, which lead to time lags and varying dynamics between the time series [27,58], are neglected or wrongly reflected by r_s . Therefore, a qualitative analysis of τ and LAI is given in the following.

5.2.2. Qualitative Comparison

Figure 11 shows the different datasets for 2012–2017. In the left column, τ_a is shown as yearly climatologies, i.e., no inter-annual variations [26]; the right column shows τ_a calculated as described by Melzer [33] and Vreugdenhil et al. [34] (VC_{dyn}). The τ_a time series retrieved with original (25°/40°) and modified (10°/30°) cross-over angles are displayed as dashed and solid lines, respectively. As can be seen in Figure 11, a change to lower cross-over angles leads to a larger range of values, i.e., a stronger vegetation signal. The value range of all τ and LAI time series is relatively similar over all years, but some inter-annual dynamics are visible, e.g., a variable number of main peaks and different timings of those peaks (Figure 11). This supports the implementation of dynamic parameters for the retrieval of τ_a in the study area. The τ_a time series shows significant inter-annual differences, which are likely to reflect different weather conditions. In the study area, 2015 was a warm and dry year, thus encouraging early vegetation growth and leading to a high peak in τ_a . In contrast, 2016 was rather wet, with light and heavy rainfalls the whole year. This is reflected by a relatively flat τ_a time series with some distinct ups and downs throughout the year.

For an interpretation of signal dynamics between years and during each growing season, we examine the reference datasets. Two main peaks occur around June and September in τ_s , which does not include inter-annual variations, and in τ_{a2} in every year. Those two peaks coincide with the peak of season in winter crops (first peak) and summer crops (second peak) and their harvest shortly after. The LAI dataset also shows these two peaks, however not as pronounced in every year. In most of the years, the rise in spring occurs later, but increases more quickly than the microwave datasets. Recurring features can also be identified in the τ_a time series: each year, τ_a starts to rise in February, shows one peak in April/May, one peak around June/July and one peak in August/September, and then drops again in autumn. The two peaks in June/July and August/September coincide with those visible in the reference datasets, however slightly shifted in time compared to LAI. This is likely due to the sensitivity of the different variables to different vegetation characteristics; since LAI is more sensitive to the green canopy, it observes peaks earlier than τ , which is more sensitive to the water content in the vegetation, including the woody parts of the canopy [34,57,59]. To test this for the datasets used in this study, correlations were calculated between the datasets after introducing negative and positive temporal shifts of 0–12 weeks. Figure 12 shows the results of the analysis, which confirm that highest r_s values are obtained when applying a positive temporal shift of two weeks (τ_s) and 6–8 weeks (τ_a , τ_{a2}) to the LAI dataset. The smaller shift between LAI and τ_s can be explained by the fact that τ_s is based on NDVI, which has been found to have a smaller phase shift to LAI than τ in several land cover regions [57]. Between τ_a and τ_{a2} , r_s is highest with no introduced time shift. Similar results are obtained for τ_s , except when correlating it with τ_a retrieved with cross-over angles 10° and 30° and

using VC_{seas} . However, all r_s values obtained between those two time series with positive temporal shifts of 0–6 weeks lie within a range of 0.10, and the maximum r_s value is not as distinct as in other dataset combinations.

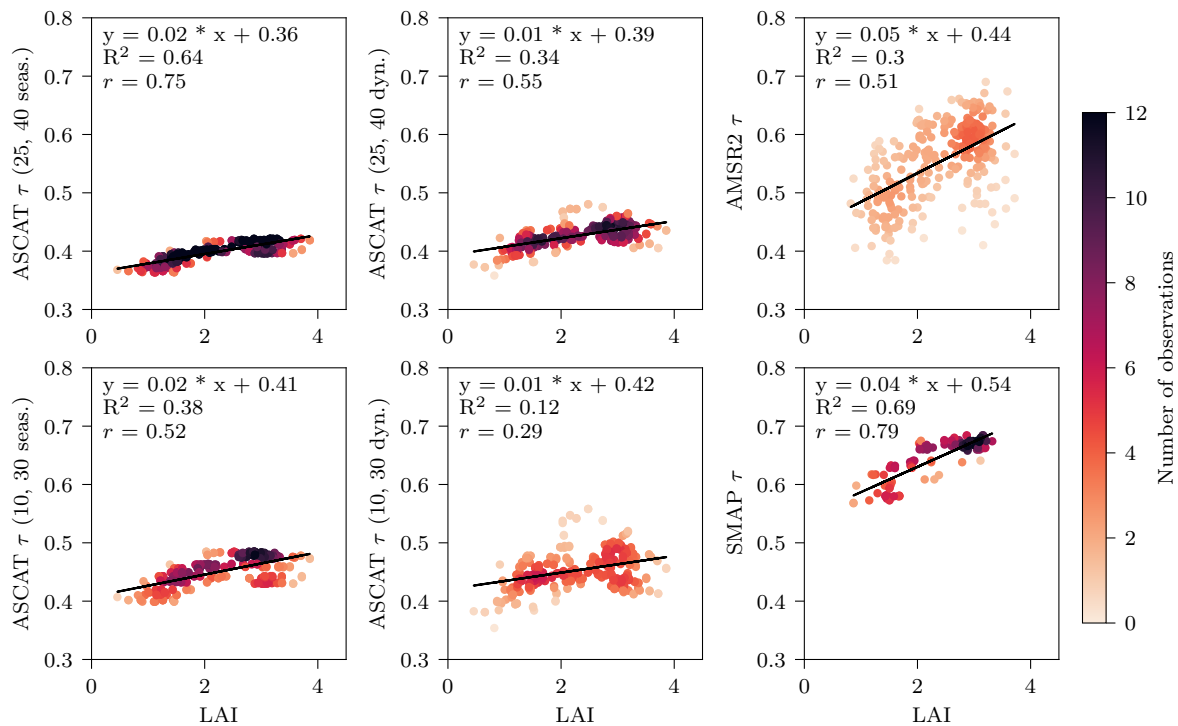


Figure 10. Satellite τ as a function of SPOT-VGT/PROBA-V LAI; the color indicates the number of observations. The black line shows the linear regression. In each panel, the function of the linear regression, the coefficient of determination (R^2) and r_s are given.

5.2.3. Land Cover Effect

Land cover in the study region is mostly cropland, but it also features grasslands and forests (mostly evergreen and mixed evergreen/deciduous). Figure 13 shows the LAI time series of up to three selected only-forest (MF, DF, EF), only-cropland (C) and only-grassland (G) areas, as well as the τ_a time series of the 25 km ASCAT footprint over the study region. The three selected cropland LAI time series (Figure 13, bottom left) show different peaks due to the planted crop type (winter crops vs. summer crops). As can be seen in the figure, dynamics in LAI and τ_a correlate well, and, as expected, features from all selected land cover types can be found in the τ_a time series of the study area. Differences in the absolute values of τ_a between the years might be caused by different temperature and rainfall conditions.

Every year, a peak is visible in the τ_a signal around April/May (Figure 11, right column). This peak is not present in LAI (Figures 11 and 13) and cannot be explained by a particular change in vegetation water content or biomass. To investigate a possible effect of remained snow or wet snow, we looked at photos taken in the HOAL catchment and analyzed meteorological data from GLDAS (air temperature, rainfall and snowfall). However, the GLDAS snowfall rate was zero in most years (see Figure 5c) and no snow was detected on the photos during the periods of interest. Snow can thus most likely be excluded as a reason for the visible peak in spring. A likely interpretation of the peak could be changes in the scattering behavior of the vegetation or bare surface due to structural changes during this period. The size of the peak varies over the years; in 2014, it is very high and wide, whereas, one year later, it is hardly present. The origin of those peaks and their amplitudes are still under investigation. Because we also see inconsistencies in spring in SM, this issue will be addressed in the Discussion Section.

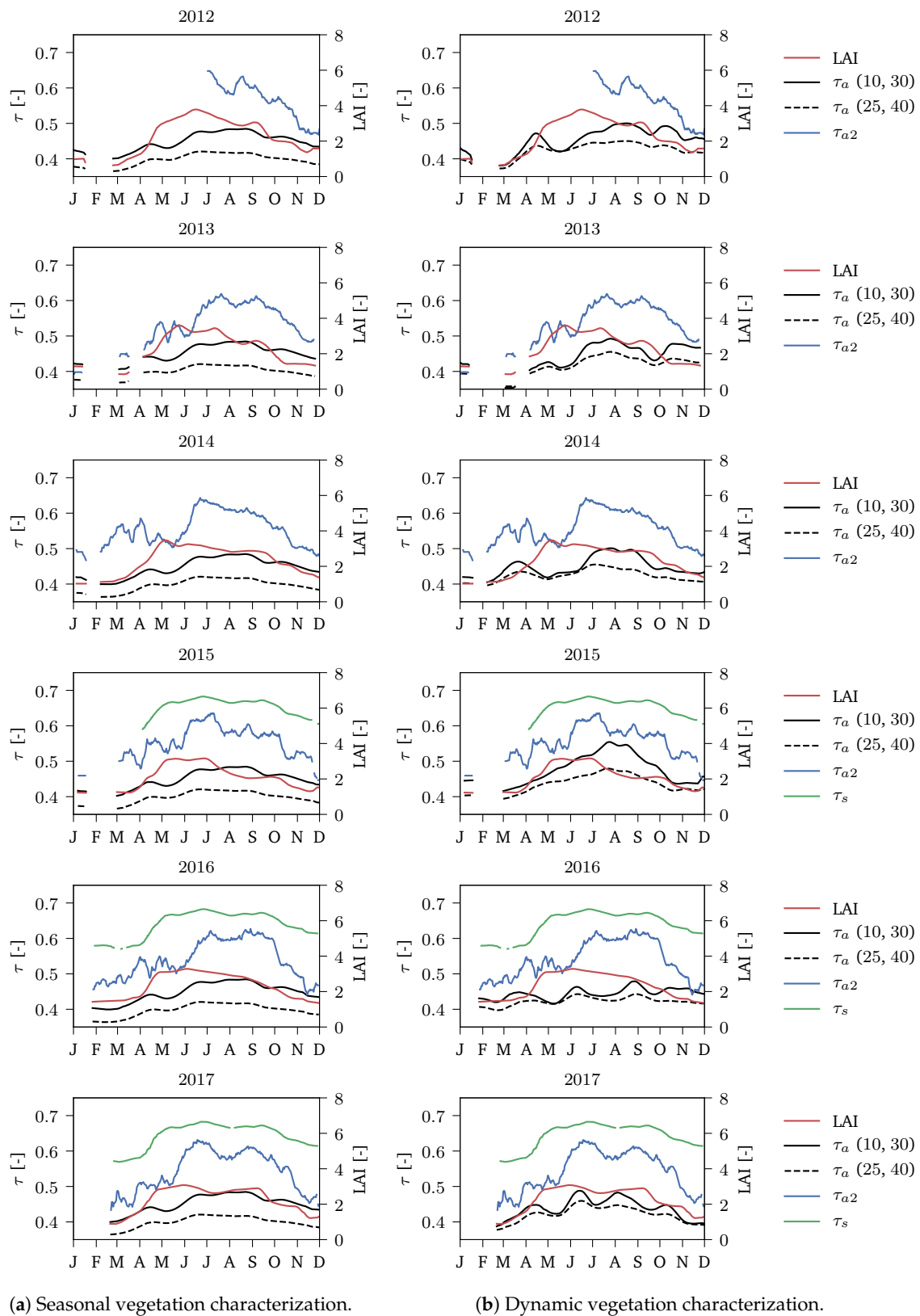


Figure 11. τ and LAI for the years 2012 to 2017; τ_a retrieved using: (a) VC_{seas} ; and (b) VC_{dyn} .

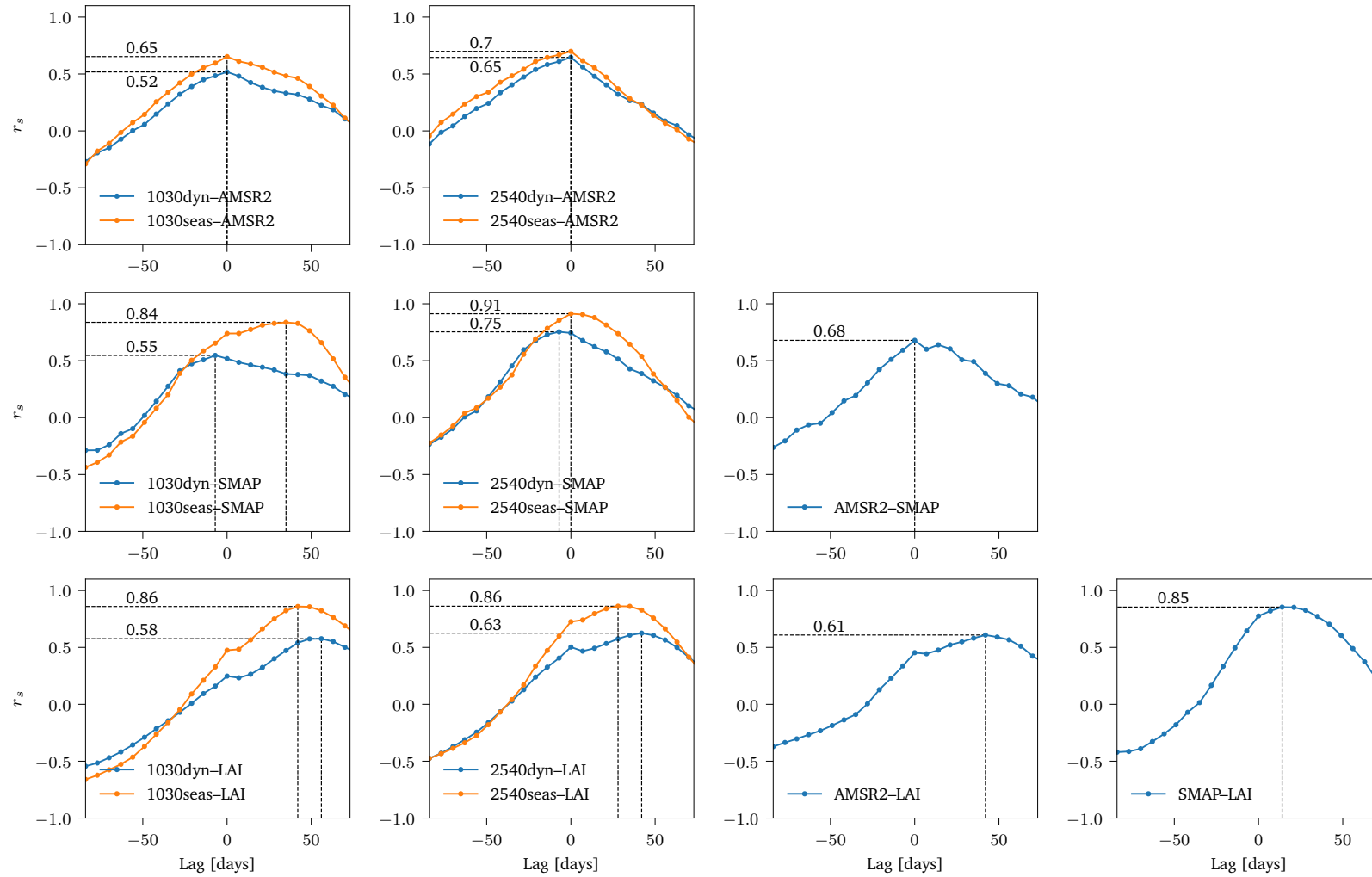


Figure 12. r_s obtained between the indicated time series after applying negative/positive temporal shifts of up to twelve weeks to the latter one.

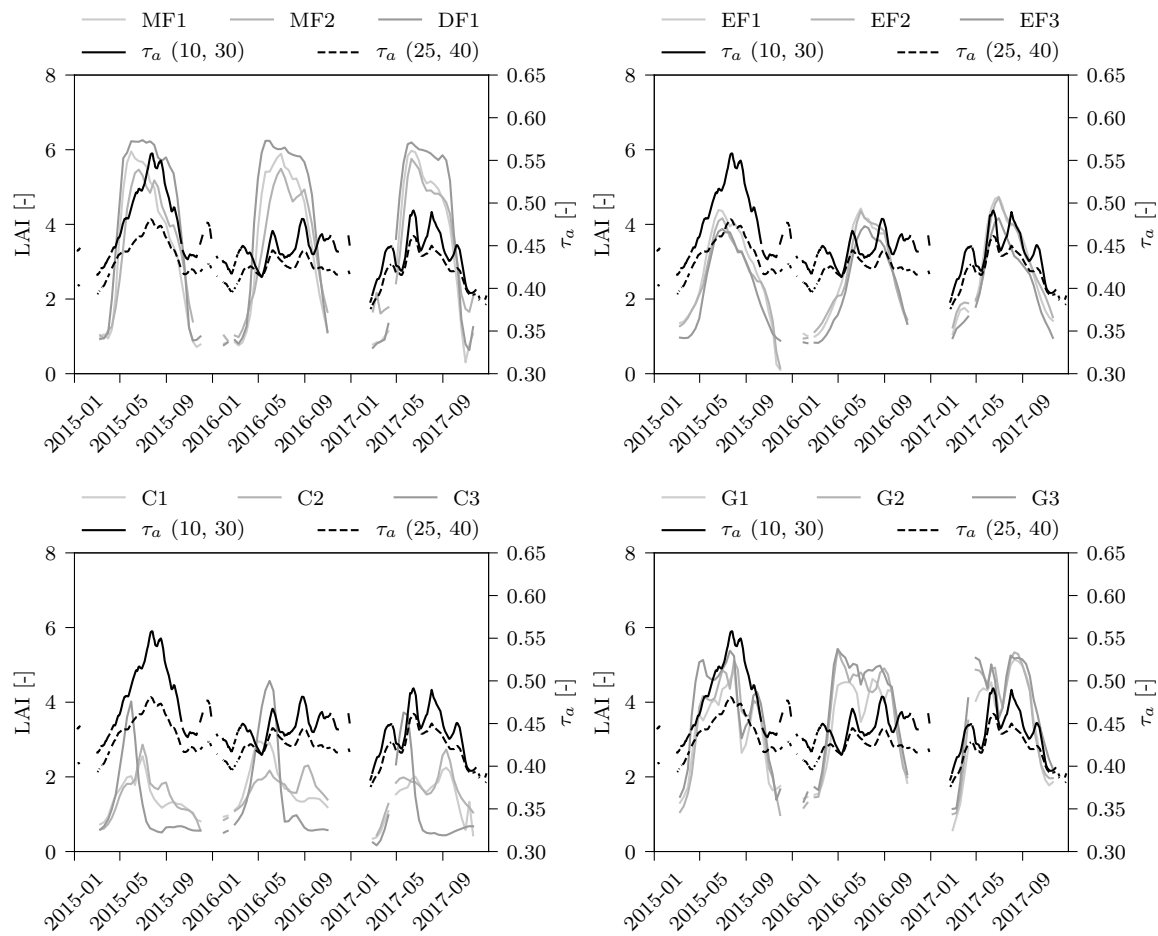


Figure 13. LAI from: (**top left**) mixed and deciduous forest (MF, DF); (**top right**) evergreen coniferous forest (EF); (**bottom left**) croplands (C); and (**bottom right**) grasslands (G); and τ_a from the study region (all panels). Frozen periods are masked out.

6. Discussion

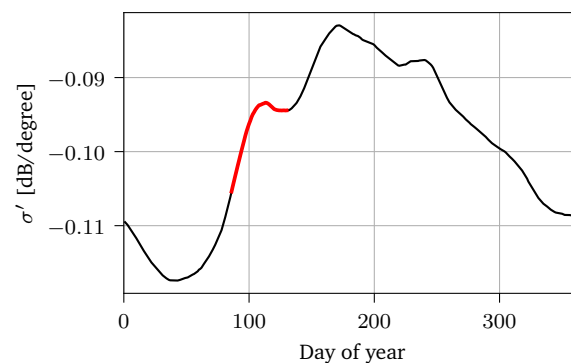
This study analyzed the effect of a regionally optimized parameterization of vegetation in the TU Wien algorithm for both the SM and τ_a products derived from Metop-A ASCAT backscatter. The analysis of SM shows that, in the study area, a stronger vegetation correction than the globally optimal parameter is needed. Correlations with reference datasets increase, and seasonal differences such as an underestimation of SM in spring and an overestimation in summer are mitigated; however, they are not fully corrected. The application of VC_{seas} or VC_{dyn} does not affect the SM dataset as much as the choice of the cross-over angles.

To transfer these findings to other regions in temperate climates and test if the problems described in Section 1 are mitigated by the application of a stronger vegetation correction, correlations and the $ubRMSD$ between ASCAT and in situ SM have been calculated for the Little River watershed (Georgia, United States; [22]), an area in southwest France [24] and a catchment in western Denmark (hydrological observatory HOBE; [60,61]). At all sites, r_p and r_s increase from 0.64 to 0.71 on average when applying a stronger vegetation correction; the average $ubRMSD$ decreases from 0.031 to 0.028. Table 2 shows the metrics for every location. The metrics have been calculated for the period 2012–2017 (LR and southwest France) and 2012–2015 (HOBE), and periods with negative temperatures or snowfall have been masked out, as described in Section 3.3.

Table 2. Metrics between different ASCAT SM versions and three in situ SM datasets.

Catchment	ASCAT Version	r_p	r_s	$ubRMSD$
LR	25/40, VC_{seas}	0.60	0.58	0.031
LR	10/30, VC_{seas}	0.68	0.68	0.025
LR	25/40, VC_{dyn}	0.61	0.59	0.030
LR	10/30, VC_{dyn}	0.64	0.63	0.026
SW France	25/40, VC_{seas}	0.62	0.64	0.035
SW France	10/30, VC_{seas}	0.67	0.69	0.033
SW France	25/40, VC_{dyn}	0.64	0.67	0.034
SW France	10/30, VC_{dyn}	0.70	0.72	0.032
HOBE	25/40, VC_{seas}	0.68	0.71	0.029
HOBE	10/30, VC_{seas}	0.77	0.79	0.026
HOBE	25/40, VC_{dyn}	0.70	0.72	0.028
HOBE	10/30, VC_{dyn}	0.79	0.78	0.025

When analyzing the τ_a time series, the added value of a dynamic vegetation parameterization becomes obvious. Inter-annual differences due to different weather conditions are visible, and vegetation dynamics such as start and peak of season and harvest of different crop types are reflected in the signal. As for SM, discrepancies between ASCAT and the reference datasets are observed in spring. This discrepancy in spring, where the effect of vegetation is over- and SM underestimated, is currently being investigated. In the course of the SM retrieval, the dependency of σ° on the incidence angle θ is modeled as a second-order Taylor polynomial (see Section 3.2.1). The first component, i.e., the slope of the σ° – θ curve (σ'), decreases (in absolute values) with vegetation growth, since volume scattering from the vegetation increases σ° at larger incidence angles (Figure 4, bottom). Figure 14 shows the time series of σ' . In addition to the main seasonal cycle of vegetation growth, we also see a peak in spring (Day of Year 85–130). This means that, during that time, the backscattered component is less dependent on the incidence angle. Behavior such as this is commonly associated with vegetation growth, but can in this case also be due to changes in the structure of the vegetation (e.g., crops growth changes from grass-like to vertical), or due to SM-induced alteration of σ' . Structural differences would induce a change in the single scattering albedo (ω), i.e., in the scattering and absorption behavior of the vegetation layer. At the moment, ω is considered to be static over time in the TU Wien retrieval algorithm. The same assumption is made in the retrieval algorithm of τ_{a2} , where we also see peaks in April. Assuming that ω shows a seasonal cycle and the effect of considering this cycle in the ASCAT SM and τ_a retrieval should be explored in further research.

**Figure 14.** Average annual behavior of the slope of the σ° – θ relationship. The peak in spring is highlighted in red.

7. Conclusions

We analyzed the retrieval of surface soil moisture (SM) and vegetation optical depth τ from Metop-A ASCAT over a region in Lower Austria. Both SM and τ have been retrieved from ASCAT backscatter values using a seasonal and a dynamic vegetation characterization, which takes into account year-to-year changes. Furthermore, the effect of adjusting parameters related to the strength of the vegetation characterization has been analyzed. We found that changing the empirically identified cross-over angles used for the global SM retrieval according to regional conditions improves the SM retrieval considerably (increase of r_s by 0.15 on average, and r_s and $ubRMSE$ comparable to SMAP and AMSR2). The vegetation product derived with a dynamic vegetation characterization compares well to τ observed by AMSR2 and SMAP, and LAI from SPOT-VGT/PROBA-V. Vegetation dynamics such as start and peak of season and harvest are reflected in the signal, however partially shifted in time, which reflects the different sensitivities of LAI and τ . The results highlight the benefits of a parameterization optimized to regional conditions for an area in the temperate climate zone.

Author Contributions: I.P. conceived and designed the experiments together with M.V., S.H. and W.W.; I.P. analyzed the data and wrote the paper; and P.S. and G.B. contributed their expertise. All authors participated in the revision of the manuscript.

Funding: Financial support has been provided by the Austrian Science Fund: Vienna Doctoral Programme on Water Resource System (DKW1219-N22).

Acknowledgments: The authors would like to acknowledge funding of the equipment in the Hydrology Open Air Laboratory (HOAL) of TU Wien, as well as Markus and Matthias Oismüller for their support with the in situ data collection. The authors would like to acknowledge financial support provided by the Austrian Science Funds (FWF) as part of the Doctoral Programme on Water Resource Systems (DK W1219-N22). They would like to thank EUMETSAT for providing Metop ASCAT data.

Conflicts of Interest: The authors declare no conflict of interest. The founding sponsors had no role in the design of the study; in the collection, analyses, or interpretation of data; in the writing of the manuscript, and in the decision to publish the results.

Abbreviations

The following abbreviations are used in this manuscript:

AMSR2	Advanced Microwave Scanning Radiometer 2
ASCAT	Advanced Scatterometer
HOAL	Hydrological Open Air Laboratory
LAI	Leaf area index
SM	Soil moisture
SMAP	Soil Moisture Active Passive
τ	Vegetation optical depth
VC_{seas}	Vegetation characterization using seasonal parameters
VC_{dyn}	Vegetation characterization using dynamic parameters

References

1. Wanders, N.; Bierkens, M.F.; de Jong, S.M.; de Roo, A.; Karssenberg, D. The benefits of using remotely sensed soil moisture in parameter identification of large-scale hydrological models. *Water Resour. Res.* **2014**, *50*, 6874–6891. [\[CrossRef\]](#)
2. Wanders, N.; Karssenberg, D.; Roo, A.D.; De Jong, S.; Bierkens, M. The suitability of remotely sensed soil moisture for improving operational flood forecasting. *Hydrol. Earth Syst. Sci.* **2014**, *18*, 2343–2357. [\[CrossRef\]](#)
3. Brocca, L.; Melone, F.; Moramarco, T.; Wagner, W.; Naeimi, V.; Bartalis, Z.; Hasenauer, S. Improving runoff prediction through the assimilation of the ASCAT soil moisture product. *Hydrol. Earth Syst. Sci.* **2010**, *14*, 1881–1893. [\[CrossRef\]](#)
4. Ling, P. A review of soil moisture sensors. *Assn. Flor. Prof. Bull.* **2004**, *886*, 22–23.
5. Soulis, K.X.; Elmaloglou, S.; Dercas, N. Investigating the effects of soil moisture sensors positioning and accuracy on soil moisture based drip irrigation scheduling systems. *Agric. Water Manag.* **2015**, *148*, 258–268. [\[CrossRef\]](#)

6. Koster, R.D.; Dirmeyer, P.A.; Guo, Z.C.; Bonan, G.; Chan, E.; Cox, P.; Gordon, C.T.; Kanae, S.; Kowalczyk, E.; Lawrence, D.; et al. Regions of strong coupling between soil moisture and precipitation. *Science* **2004**, *305*, 1138–1140. [[CrossRef](#)] [[PubMed](#)]
7. Brocca, L.; Massari, C.; Ciabatta, L.; Moramarco, T.; Penna, D.; Zuecco, G.; Pianezzola, L.; Borga, M.; Matgen, P.; Martínez-Fernández, J. Rainfall estimation from in situ soil moisture observations at several sites in Europe: An evaluation of the SM2RAIN algorithm. *J. Hydrol. Hydromech.* **2015**, *63*, 201–209. [[CrossRef](#)]
8. Svoboda, M.; LeComte, D.; Hayes, M.; Heim, R.; Gleason, K.; Angel, J.; Rippey, B.; Tinker, R.; Palecki, M.; Stooksbury, D.; et al. The drought monitor. *Bull. Am. Meteorol. Soc.* **2002**, *83*, 1181–1190. [[CrossRef](#)]
9. Hao, Z.; AghaKouchak, A. A nonparametric multivariate multi-index drought monitoring framework. *J. Hydrometeorol.* **2014**, *15*, 89–101. [[CrossRef](#)]
10. Martínez-Fernández, J.; González-Zamora, A.; Sánchez, N.; Gumuzzio, A.; Herrero-Jiménez, C. Satellite soil moisture for agricultural drought monitoring: Assessment of the SMOS derived Soil Water Deficit Index. *Remote Sens. Environ.* **2016**, *177*, 277–286. [[CrossRef](#)]
11. Rodell, M.; Velicogna, I.; Famiglietti, J.S. Satellite-based estimates of groundwater depletion in India. *Nature* **2009**, *460*, 999. [[CrossRef](#)] [[PubMed](#)]
12. Wagner, W.; Hahn, S.; Kidd, R.; Melzer, T.; Bartalis, Z.; Hasenauer, S.; Figa-Saldaña, J.; de Rosnay, P.; Jann, A.; Schneider, S.; et al. The ASCAT soil moisture product: A review of its specifications, validation results, and emerging applications. *Meteorol. Z.* **2013**, *22*, 5–33. [[CrossRef](#)]
13. Wagner, W.; Dorigo, W.; de Jeu, R.; Fernandez, D.; Benveniste, J.; Haas, E.; Ertl, M. Fusion of active and passive microwave observations to create an essential climate variable data record on soil moisture. *ISPRS Ann. Photogramm. Remote Sens. Spat. Inf. Sci.* **2012**, *7*, 315–321.
14. Kerr, Y.H.; Waldteufel, P.; Wigneron, J.P.; Martinuzzi, J.; Font, J.; Berger, M. Soil moisture retrieval from space: The Soil Moisture and Ocean Salinity (SMOS) mission. *IEEE Trans. Geosci. Remote Sens.* **2001**, *39*, 1729–1735. [[CrossRef](#)]
15. Entekhabi, D.; Njoku, E.G.; O'Neill, P.E.; Kellogg, K.H.; Crow, W.T.; Edelstein, W.N.; Entin, J.K.; Goodman, S.D.; Jackson, T.J.; Johnson, J.; et al. The soil moisture active passive (SMAP) mission. *Proc. IEEE* **2010**, *98*, 704–716. [[CrossRef](#)]
16. Parinussa, R.M.; Holmes, T.R.; Wanders, N.; Dorigo, W.A.; de Jeu, R.A. A preliminary study toward consistent soil moisture from AMSR2. *J. Hydrometeorol.* **2015**, *16*, 932–947. [[CrossRef](#)]
17. Wagner, W.; Lemoine, G.; Rott, H. A method for estimating soil moisture from ERS scatterometer and soil data. *Remote Sens. Environ.* **1999**, *70*, 191–207. [[CrossRef](#)]
18. Naeimi, V.; Scipal, K.; Bartalis, Z.; Hasenauer, S.; Wagner, W. An improved soil moisture retrieval algorithm for ERS and METOP scatterometer observations. *IEEE Trans. Geosci. Remote Sens.* **2009**, *47*, 1999–2013. [[CrossRef](#)]
19. Matgen, P.; Heitz, S.; Hasenauer, S.; Hissler, C.; Brocca, L.; Hoffmann, L.; Wagner, W.; Savenije, H. On the potential of MetOp ASCAT-derived soil wetness indices as a new aperture for hydrological monitoring and prediction: A field evaluation over Luxembourg. *Hydrol. Process.* **2012**, *26*, 2346–2359. [[CrossRef](#)]
20. Albergel, C.; Rüdiger, C.; Carrer, D.; Calvet, J.C.; Fritz, N.; Naeimi, V.; Bartalis, Z.; Hasenauer, S. An evaluation of ASCAT surface soil moisture products with in-situ observations in Southwestern France. *Hydrol. Earth Syst. Sci.* **2009**, *13*, 115–124. [[CrossRef](#)]
21. Brocca, L.; Hasenauer, S.; Lacava, T.; Melone, F.; Moramarco, T.; Wagner, W.; Dorigo, W.; Matgen, P.; Martínez-Fernández, J.; Llorens, P.; et al. Soil moisture estimation through ASCAT and AMSR-E sensors: An intercomparison and validation study across Europe. *Remote Sens. Environ.* **2011**, *115*, 3390–3408. [[CrossRef](#)]
22. Wagner, W.; Brocca, L.; Naeimi, V.; Reichle, R.; Draper, C.; de Jeu, R.; Ryu, D.; Su, C.H.; Western, A.; Calvet, J.C.; et al. Clarifications on the “Comparison between SMOS, VUA, ASCAT, and ECMWF soil moisture products over four watersheds in US”. *IEEE Trans. Geosci. Remote Sens.* **2014**, *52*, 1901–1906. [[CrossRef](#)]
23. Gruhier, C.; Rosnay, P.D.; Hasenauer, S.; Holmes, T.; De Jeu, R.; Kerr, Y.; Mougin, E.; Njoku, E.; Timouk, F.; Wagner, W.; et al. Soil moisture active and passive microwave products: Intercomparison and evaluation over a Sahelian site. *Hydrol. Earth Syst. Sci.* **2009**, *14*, 141–156. [[CrossRef](#)]

24. Barbu, A.; Calvet, J.C.; Mahfouf, J.F.; Lafont, S. Integrating ASCAT surface soil moisture and GEOV1 leaf area index into the SURFEX modelling platform: A land data assimilation application over France. *Hydrol. Earth Syst. Sci.* **2014**, *18*, 173–192. [[CrossRef](#)]
25. Hahn, S.; Reimer, C.; Vreugdenhil, M.; Melzer, T.; Wagner, W. Dynamic characterization of the incidence angle dependence of backscatter using metop ASCAT. *IEEE J. Sel. Top. Appl. Earth Obs. Remote Sens.* **2017**, *10*, 2348–2359. [[CrossRef](#)]
26. Vreugdenhil, M.; Dorigo, W.A.; Wagner, W.; de Jeu, R.A.; Hahn, S.; van Marle, M.J. Analyzing the Vegetation Parameterization in the TU-Wien ASCAT Soil Moisture Retrieval. *IEEE Trans. Geosci. Remote Sens.* **2016**, *54*, 3513–3531. [[CrossRef](#)]
27. Liu, Y.Y.; de Jeu, R.A.; McCabe, M.F.; Evans, J.P.; van Dijk, A.I. Global long-term passive microwave satellite-based retrievals of vegetation optical depth. *Geophys. Res. Lett.* **2011**, *38*. [[CrossRef](#)]
28. Tian, F.; Brandt, M.; Liu, Y.Y.; Verger, A.; Tagesson, T.; Diouf, A.A.; Rasmussen, K.; Mbow, C.; Wang, Y.; Fensholt, R. Remote sensing of vegetation dynamics in drylands: Evaluating vegetation optical depth (VOD) using AVHRR NDVI and in situ green biomass data over West African Sahel. *Remote Sens. Environ.* **2016**, *177*, 265–276. [[CrossRef](#)]
29. Blöschl, G.; Blaschke, A.; Broer, M.; Bucher, C.; Carr, G.; Chen, X.; Eder, A.; Exner-Kittridge, M.; Farnleitner, A.; Flores-Orozco, A.; et al. The Hydrological Open Air laboratory (HOAL) in Petzenkirchen: A hypothesis-driven observatory. *Hydrol. Earth Syst. Sci.* **2016**, *20*, 227. [[CrossRef](#)]
30. Bontemps, S.; Defourny, P.; Radoux, J.; Van Bogaert, E.; Lamarche, C.; Achard, F.; Mayaux, P.; Boettcher, M.; Brockmann, C.; Kirches, G.; et al. Consistent global land cover maps for climate modelling communities: Current achievements of the ESA's land cover CCI. In Proceedings of the ESA Living Planet Symposium, Edinburgh, UK, 9–13 September 2013; pp. 9–13.
31. Wagner, W.; Noll, J.; Borgeaud, M.; Rott, H. Monitoring soil moisture over the Canadian Prairies with the ERS scatterometer. *IEEE Trans. Geosci. Remote Sens.* **1999**, *37*, 206–216. [[CrossRef](#)]
32. Wagner, W.; Lemoine, G.; Borgeaud, M.; Rott, H. A study of vegetation cover effects on ERS scatterometer data. *IEEE Trans. Geosci. Remote Sens.* **1999**, *37*, 938–948. [[CrossRef](#)]
33. Melzer, T. Vegetation modelling in WARP 6.0. In Proceedings of the EUMETSAT Meteorological Satellite Conference, Vienna, Austria, 16–20 September 2013; pp. 1–7.
34. Vreugdenhil, M.; Hahn, S.; Melzer, T.; Bauer-Marschallinger, B.; Reimer, C.; Dorigo, W.A.; Wagner, W. Assessing vegetation dynamics over mainland Australia with metop ASCAT. *IEEE J. Sel. Top. Appl. Earth Obs. Remote Sens.* **2017**, *10*, 2240–2248. [[CrossRef](#)]
35. Owe, M.; de Jeu, R.; Holmes, T. Multisensor historical climatology of satellite-derived global land surface moisture. *J. Geophys. Res. Earth Surf.* **2008**, *113*. [[CrossRef](#)]
36. Kim, S.; Liu, Y.Y.; Johnson, F.M.; Parinussa, R.M.; Sharma, A. A global comparison of alternate AMSR2 soil moisture products: Why do they differ? *Remote Sens. Environ.* **2015**, *161*, 43–62. [[CrossRef](#)]
37. Zreda, M.; Shuttleworth, W.; Zeng, X.; Zweck, C.; Desilets, D.; Franz, T.; Rosolem, R. COSMOS: The cosmic-ray soil moisture observing system. *Hydrol. Earth Syst. Sci.* **2012**, *16*, 4079–4099. [[CrossRef](#)]
38. Cho, E.; Su, C.H.; Ryu, D.; Kim, H.; Choi, M. Does AMSR2 produce better soil moisture retrievals than AMSR-E over Australia? *Remote Sens. Environ.* **2017**, *188*, 95–105. [[CrossRef](#)]
39. Kim, S.; Kim, H.; Choi, M. Evaluation of satellite-based soil moisture retrieval over the Korean peninsula: Using AMSR2 LPRM algorithm and ground measurement data. *J. Korea Water Resour. Assoc.* **2016**, *49*, 423–429. [[CrossRef](#)]
40. Anoop, S.; Maurya, D.K.; Rao, P.; Sekhar, M. Validation and Comparison of LPRM Retrieved Soil Moisture Using AMSR2 Brightness Temperature at Two Spatial Resolutions in the Indian Region. *IEEE Geosci. Remote Sens. Lett.* **2017**, *14*, 1561–1564. [[CrossRef](#)]
41. Yee, M.S.; Walker, J.P.; Rüdiger, C.; Parinussa, R.M.; Koike, T.; Kerr, Y.H. A comparison of SMOS and AMSR2 soil moisture using representative sites of the OzNet monitoring network. *Remote Sens. Environ.* **2017**, *195*, 297–312. [[CrossRef](#)]
42. Cui, C.; Xu, J.; Zeng, J.; Chen, K.S.; Bai, X.; Lu, H.; Chen, Q.; Zhao, T. Soil moisture mapping from satellites: An intercomparison of SMAP, SMOS, FY3B, AMSR2, and ESA CCI over two dense network regions at different spatial scales. *Remote Sens.* **2017**, *10*, 33. [[CrossRef](#)]

43. Han, E.; Crow, W.; Holmes, T.; Bolten, J. Relative Skills of Soil Moisture and Vegetation Optical Depth Retrievals for Agricultural Drought Monitoring. In *AGU Fall Meeting Abstracts*; American Geophysical Union: San Francisco, CA, USA, 2012.
44. Liu, Y.Y.; Dijk, A.I.; McCabe, M.F.; Evans, J.P.; Jeu, R.A. Global vegetation biomass change (1988–2008) and attribution to environmental and human drivers. *Glob. Ecol. Biogeogr.* **2013**, *22*, 692–705. [[CrossRef](#)]
45. Schmugge, T.; Gloersen, P.; Wilheit, T.; Geiger, F. Remote sensing of soil moisture with microwave radiometers. *J. Geophys. Res.* **1974**, *79*, 317–323. [[CrossRef](#)]
46. Njoku, E.G.; Entekhabi, D. Passive microwave remote sensing of soil moisture. *J. Hydrol.* **1996**, *184*, 101–129. [[CrossRef](#)]
47. Konings, A.G.; Piles, M.; Das, N.; Entekhabi, D. L-band vegetation optical depth and effective scattering albedo estimation from SMAP. *Remote Sens. Environ.* **2017**, *198*, 460–470. [[CrossRef](#)]
48. Colliander, A.; Jackson, T.; Bindlish, R.; Chan, S.; Das, N.; Kim, S.; Cosh, M.; Dunbar, R.; Dang, L.; Pashaian, L.; et al. Validation of SMAP surface soil moisture products with core validation sites. *Remote Sens. Environ.* **2017**, *191*, 215–231. [[CrossRef](#)]
49. Chan, S.K.; Bindlish, R.; O'Neill, P.E.; Njoku, E.; Jackson, T.; Colliander, A.; Chen, F.; Burgin, M.; Dunbar, S.; Piepmeier, J.; et al. Assessment of the SMAP passive soil moisture product. *IEEE Trans. Geosci. Remote Sens.* **2016**, *54*, 4994–5007. [[CrossRef](#)]
50. Chan, S.; Hunt, R.; Bindlish, R.; Njoku, E.; Kimball, J.; Jackson, T. Ancillary Data Report for Vegetation Water Content. SMAP Proj. Doc., JPL D-53061. SMAP Data Documents. 2013. Available online: https://smap.jpl.nasa.gov/system/internal_resources/details/original/289_047_veg_water.pdf (accessed on 10 November 2018).
51. Dierckx, W.; Sterckx, S.; Benhadj, I.; Livens, S.; Duhoux, G.; Van Achteren, T.; Francois, M.; Mellab, K.; Saint, G. PROBA-V mission for global vegetation monitoring: Standard products and image quality. *Int. J. Remote Sens.* **2014**, *35*, 2589–2614. [[CrossRef](#)]
52. Rodell, M.; Houser, P.; Jambor, U.; Gottschalk, J.; Mitchell, K.; Meng, C.; Arsenault, K.; Cosgrove, B.; Radakovich, J.; Bosilovich, M.; et al. The Global Land Data Assimilation System. *Bull. Am. Meteorol. Soc.* **2004**, *85*, 381–394. [[CrossRef](#)]
53. Bartalis, Z.; Wagner, W.; Naeimi, V.; Hasenauer, S.; Scipal, K.; Bonekamp, H.; Figa, J.; Anderson, C. Initial soil moisture retrievals from the METOP-A Advanced Scatterometer (ASCAT). *Geophys. Res. Lett.* **2007**, *34*. [[CrossRef](#)]
54. Albergel, C.; Rüdiger, C.; Pellarin, T.; Calvet, J.C.; Fritz, N.; Froissard, F.; Suquia, D.; Petitpa, A.; Piguet, B.; Martin, E. From near-surface to root-zone soil moisture using an exponential filter: An assessment of the method based on in-situ observations and model simulations. *Hydrol. Earth Syst. Sci. Discuss.* **2008**, *12*, 1323–1337. [[CrossRef](#)]
55. Wagner, W. Soil Moisture Retrieval from ERS Scatterometer Data. Ph.D. Thesis, Citeseer, Vienna, Austria, 1998.
56. Lawrence, H.; Wigneron, J.P.; Richaume, P.; Novello, N.; Grant, J.; Mialon, A.; Al Bitar, A.; Merlin, O.; Guyon, D.; Leroux, D.; et al. Comparison between SMOS Vegetation Optical Depth products and MODIS vegetation indices over crop zones of the USA. *Remote Sens. Environ.* **2014**, *140*, 396–406. [[CrossRef](#)]
57. Jones, M.O.; Jones, L.A.; Kimball, J.S.; McDonald, K.C. Satellite passive microwave remote sensing for monitoring global land surface phenology. *Remote Sens. Environ.* **2011**, *115*, 1102–1114. [[CrossRef](#)]
58. Jones, M.O.; Kimball, J.S.; Jones, L.A. Satellite microwave detection of boreal forest recovery from the extreme 2004 wildfires in Alaska and Canada. *Glob. Chang. Biol.* **2013**, *19*, 3111–3122. [[CrossRef](#)] [[PubMed](#)]
59. Jones, M.O.; Kimball, J.S.; Jones, L.A.; McDonald, K.C. Satellite passive microwave detection of North America start of season. *Remote Sens. Environ.* **2012**, *123*, 324–333. [[CrossRef](#)]
60. Jensen, K.H.; Illangasekare, T.H. HOBE: A hydrological observatory. *Vadose Zone J.* **2011**, *10*, 1–7. [[CrossRef](#)]
61. Bircher, S.; Skou, N.; Jensen, K.H.; Walker, J.P.; Rasmussen, L. A soil moisture and temperature network for SMOS validation in Western Denmark. *Hydrol. Earth Syst. Sci.* **2012**, *16*, 1445–1463. [[CrossRef](#)]

